Inferior Alveolar Canal Segmentation in Cone Beam Computed Tomography Images using an Adaptive Diffusion Flow Active Contour Model

Chadaporn Keatmanee [1,2], Stanislav S. Makhanov [1], Kazunori Kotani [2], Toshiaki Kondo [1], Saowapak S. Thongvigitmanee [3]

[1] Sirindhorn International Institute of Technology (SIIT), PathumThani, Thailand.
chadaphone@gmail.com, makhanov@siit.tu.ac.th, tkondo@siit.tu.ac.th
[2] Japan Advanced Institute of Science and Technology (JAIST), Ishikawa, Japan.
ikko@jaist.ac.jp
[3] National Electronics and Computer Technology Center (NECTEC), Pathumthani,Thailand.
saowapak.thongvigitmanee@nectec.or.th

Abstract

The success of dental implant surgery is subject to accurate advanced planning. In order to properly plan for suitable implant placement, it is necessary for accurate segmentation of the inferior alveolar canal. This paper presents a new approach of a semi-automatic method based on a new and effective active contour model viz. an adaptive diffusion flow active contour model. Cone-beam computed tomography (CBCT) images is used as a dataset to extract different views of an inferior alveolar canal. The method has been tested in a ground truth set and evaluated using three similar indicators (the Jaccard index, Dice's coefficient, and Overlap coefficient), achieving promising results in all of them (0.908±0.016, 0.947±0.008, and 0.954±0.008, respectively). Moreover, the presented results show that our method obtains higher accuracy values when compared with GVF snake. The method has proven to be significantly accurate and is possibly integrable in current dental implant surgery planning systems.

1 Introduction

A 3-dimensional (3D) dataset acquired from cone-beam computed tomography (CBCT) has become one of the most important dental radiographies for diagnosis of dental and maxillofacial applications [10]. For example, it is applied to dental implant planning: a surgical component which provides an artificial root by means of interfacing with the bone of the jaw (mandible) to support dental prosthesis.

In order to make accurate implant site assessment, the effective visualization system of dental radiography is strongly demanded by dentists. Especially, it could help to reduce the risk of injury to the inferior alveolar nerve (IAN), that affects a sensation system and may cause infection as well as failure to osseointegrate [3]. Due to the position of the IAN traveling within the inferior alveolar canal (IAC) in the mandible, the IAC is more detectable than the IAN itself. Therefore, robust segmentation of the inferior alveolar canal (IAC) is one of the key features to be improved in dental radiography applications.

The aim of this paper is to detect and reconstruct the main feature of IAC using a new and effective active contour model viz. an adaptive diffusion flow active contour model (ADF snake) applied to the CBCT dataset. This paper demonstrates how the algorithm can generate an extremely suitable vector field for a deformable process of the active contour model, to get a well segmented feature of the IAC on each slide of the dataset. Especially, when the IAC passes across the spongious region. Besides segmentation, the ADF snake is applied as a tracking method to get full structure of the IAC in the 3D dataset.

2 Related Work

Many dental applications have carried out the process of 3D reconstruction from a CT or CBCT dataset by de-emphasizing IAC segmentation as in [6] and [9]; they detected IAC based on panoramic CT images by reforming the stack of original CT images. The segmented results and its visualization of the IAC using the panoramic method may not be very much satisfactory. Another approach [2] presented an IAC based on a geodesic active contour model, the level set method. The main disadvantages of the model is that it has to follow three conditions: the tabular structure consists of only one connected component, not close to other component, and no self-intersections the structure. Beside these conditions, the model may not perform well under the real situation based on the deformable function. A state of the art algorithm, the GVF snake was also implemented in [13] for quantitative image reconstruction applied to mandibular distraction. This paper mostly demonstrated the optimization of the key parameters of the GVF snake as well. Beside the above cited methods, there are various other methods implemented for IAC detection including [1], [5], and [7].

3 Theoretical Background

An active contour model [4] has been expansively implemented in image processing and computer vision owing to its proficient performance. Also, there have been many studies that try to overcome its disadvantages including the method applied in this study, a new and effective ADF active contour model (ADF snake). This section aims at simplifying the explanation of an ADF snake as explained below:

An Adaptive Diffusion Active Contour Model

An ADF snake is a new and effective external force [14] developed to solve problems in previous snakes including low capture range, weak edge leaking, as well as deep and narrow concavity regions. This framework is established as an equivalent framework between the GVF snake diffusion process [16] and the image restoration process. The improved features can be described as follows;

For simplicity of theoretical explanation, the GVF energy is rewritten as

$$E(u,v) = \iint \mu \cdot \Phi(|\nabla \mathbf{v}|)dxdy + \iint |\mathbf{v} - \nabla f|^2 dxdy. \quad (1)$$

1. Weak edge leaking: by considering the GVF snake, in the smoothness energy, the vector field is smoothed in the direction of gradient as same as in the edge direction which is undesired. In order to preserve a weak edge, there should be no diffusion parallel to the gradient. Hence, in ADF *a hypersurface minimal function*: $\Phi(\nabla V) = \sqrt{1 + |\nabla \mathbf{v}|^2}$ is substituted in the smoothness energy term in the GVF snake. The function is preferable to diffuse along the tangent direction of an edge so that the weak edge is preserved efficiently. When consider $\mathbf{v}$ as a surface defined on image domain, the corresponding diffusion term in GVF is given by

$$E(u,v) = \iint \sqrt{1 + |G_\sigma \otimes \nabla \mathbf{v}|^2} dxdy \quad (2)$$

where G_σ is the Gaussian kernel of standard deviation σ which could smooth the vector field, $\nabla \mathbf{v}$ presents the gradient of $\mathbf{v}$, and $\otimes$ denotes the convolution operator.

2. Adaptive diffusion force filed: using *harmonic maps*: $p(|\nabla f|) = 1 + 1/(1 + |\nabla G_\sigma \otimes f(x)|)$ which ranges from 1 to 2. Consequently, the diffusion process of the force field can be adjusted adaptively according to image characteristics so it can preserve weak edges and smooth force filed. Thus, the *harmonic hypersurface function* is defined as

$$E(u,v) = \iint \frac{1}{p(|\nabla f|)} (\sqrt{1 + |G_\sigma \otimes \nabla \mathbf{v}|^2})^{p(|\nabla f|)} d\Omega. \quad (3)$$

where Ω is a bounded open subset of $\Re^2$, $\partial\Omega$ denotes its boundary and f presents an edge map.

3. Converge to narrow and deep concavity: developed *Infinity Laplacian function* to encourage the diffusion along the normal direction in the image smoothing region so as to make vectors downward into the boundary concavity instead of converging from two opposite directions. The function is given by

$$E(p \to \infty)(u,v) = \frac{1}{p} \int_\Omega |\nabla \mathbf{v}|_{L^\infty(\Omega)} d\Omega. \quad (4)$$

(a) (b)

Figure 1. An example of IAC enhancement image. (a) Original image.; (b) Enhanced image.

Finally, a unified diffusion framework, called *adaptive diffusion flow (ADF)* is given by

$$E_p(u,v) = \iint g \cdot (-m \cdot \Theta_{L^\infty(\Omega)} + (1-m) \cdot \frac{1}{p(|\nabla f|)} \cdot (\sqrt{1+\Omega})^{p(|\nabla f|)}) dxdy + \iint h \cdot (|\mathbf{v} - \nabla f|^2) dxdy \quad (5)$$

where $\Theta = |G_\sigma \otimes \nabla \mathbf{v}|^2$, g and h are weighting functions (same as GGVF [15]); $g(\nabla f) = e^{-(\frac{|\nabla f|}{K})}$ (K is the weighting parameter determining to some extent degree of tradeoff between field smoothness and gradient conformity), $h(|\nabla f|) = 1 - g(|\nabla f|)$, and m is also the weighting function which is given by

$$m = \begin{cases} [1 - f^2/5K^2]^2 & \text{if } f^2/5 \le K^2 \\ 0 & \text{otherwise.} \end{cases}$$

here, $K = 1.4826 \cdot E(||\nabla f| - E(|\nabla f|)|)$ and $E(\cdot)$ presents the mean value.

4 Inferior Alveolar Canal Segmentation

Segmentation of an IAC is still challenging due to an imperfect of the dataset (CBCT) including noise, low contrast, and broken boundaries. Especially, when considering all drawbacks of previous methods and the effective performance of the ADF snake as mentioned earlier, the ADF snake stands out to be one of the proficient methods for IAC segmentation.

4.1 Materials

The CBCT data were provided by the Dental cone-beam CT Scanner (DentiiScan) [11] and [12]. CBCT volumes are comprised of slices of size 400×400 pixels, with resolutions of $\Delta x = \Delta y = \Delta z = 0.4mm$. The number of slices is 323 in each patient.

4.2 Image Enhancement

Based on the imperfect of the dataset, that are noisy, low in contrast, and with broken boundaries, image enhancement is needed before the segmentation process. The morphological operations (top-hat and bottom-hat) were applied to the dataset for edge enhancement and noise suppression as shown in Figure 1. By letting $f : E \mapsto \Re^2$ be a grayscale image, and $b(x)$ be a grayscale structuring element, the enhanced image is

$$f_{enhance} = f + (f - f \circ b) - (f \bullet b - f).$$

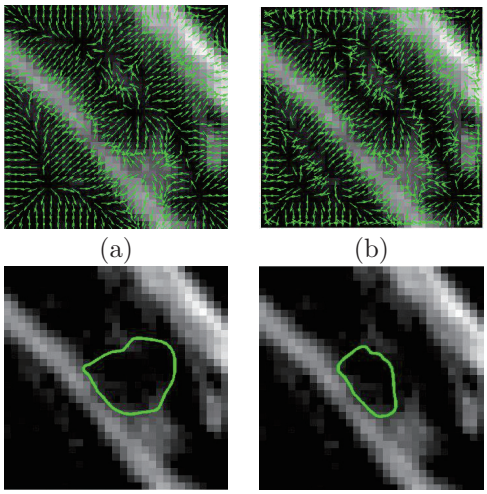

Figure 2. The comparison of IAC segmentation between the GVF snake and the ADF snake focusing on weak edge leaking convergence. (a) GVF force field; (b) ADF force field; (c) GVF snake segmentation result; (d) ADF snake segmentation result; Both models use the same parameters for deformation, $\alpha = 0.1$, $\beta = 1$, $iteration = 60$.

4.3 Segmentation and Tracking Process

The significant property of the ADF snake for IAC segmentation is that it can create a suitable vector field for snake deformation based on the image characteristics; for example weak edge, disconnected, and strong adjacent boundaries. The comparison of vector fields and segmented boundaries between well-known algorithms, the GVF snake and the ADF snake are shown in Figure 4.3. It can be noted the ADF snake performs very much better than the GVF snake. By considering the force field, ADF force field's direction is more parallel to the IAC boundaries than the force field of GVF because the ADF force field is calculated in both normal and tangent directions whereas the GVF force field is computed in only normal direction.

An ADF snake was used for an IAC segmentation, slice by slice, and then reconstruct it for 3D visualization. Besides segmentation, the active contour model has significant performance for object tracking. Therefore, the ADF snake is applied as a tracking method by user intervention in the first and last slices for contour initialization and at the end of tracking process respectively. In between both slices, the ADF snake is applied to the current segmented results to be an initial contour of the next slice. The procedure for the IAC segmentation and tracking is described in the flowchart as shown in Figure 3.

4.4 3D Reconstruction

The segmented CBCT results are visualized in 3D volume rendering by CBCT image viewer: DentiView version 3.0 (NECTEC, Thailand) [8]. An example of 3D reconstruction of a patient's IACs in the right and left sides are shown in Figure 5.

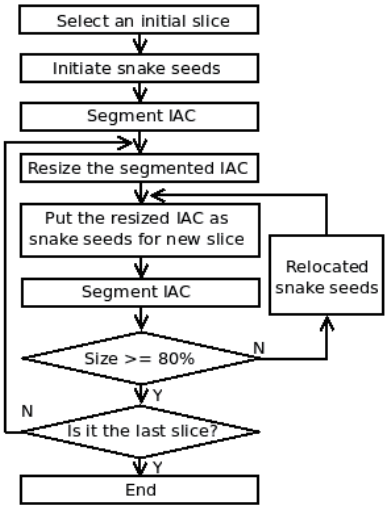

Figure 3. A flowchart for segmentation and tracking of the ADF snake to find IACs in a 3D dataset.

Figure 4. An example IAC segmentation by ADF snake and its ground truth. (a) An original IAC image; (b) The bright contour depicts a result of an IAC segmentation by ADF snake ; (c) The apparent contour expresses a ground truth of an IAC.

4.5 Data Analysis

In order to evaluate the accuracy of the segmentation process, 6 CBCT data were considered. The ground truth was manually segmented (randomly) in 6 hemimandibles which consisted of 240-303 cross-sections. An example of the segmented result and its ground truth are shown in Figure 4.

There are 3 different indicators of similarity used for comparing the cross-sections segmented by the proposed method with the ground truth;

- Jaccard index (JI)

$$JI(I_{seg}, I_{gt}) = \frac{|I_{seg} \cap I_{gt}|}{|I_{seg} \cup I_{gt}|}, \text{ where } 0 \leq JI \leq 1$$

- Dice's coefficient (DC)

$$DC(I_{seg}, I_{gt}) = \frac{2|I_{seg} \cap I_{gt}|}{|I_{seg}| + |I_{gt}|}, \text{ where } 0 \leq DC \leq 1$$

- Overlap coefficient (OC)

$$OC(I_{seg}, I_{gt}) = \frac{|I_{seg} \cap I_{gt}|}{min(|I_{seg}|, |I_{gt}|)}, \text{ where } 0 \leq OC \leq 1$$

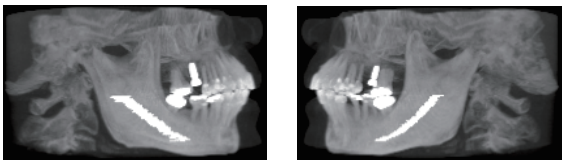

(a) (b)

Figure 5. 3D reconstruction of IAC from segmented cross-sections. (a) and (b) are the IACs at the right and left sides of the patient.

Table 1. Mean values for the analyzed indicators.

ADF snake	JI	DC	OC
Mean(μ)	0.9087	0.9472	0.9542
S.D.(σ)	0.0162	0.0087	0.0086
GVF snake			
Mean(μ)	0.7617	0.7998	0.8097
S.D.(σ)	0.0189	0.094	0.0094

5 Results and Discussion

The six datasets were measured with 3 similarity indicators as shown in Section 4.5, and the mean values as well as the standard deviation for all cases are shown in Table 1.

According to the dataset, the segmentation process is performed in cross-sectional images and the evaluation of the method has focused on studying the 2D segmentation in the cross-sections. Therefore, the evaluation strategy is based on the comparison of processed images with ground truth sets.

The results of the presented method in the described dataset have been promising in all the considered similarity indicators. Considering the overlap indicators, the method has achieved high values in the processed dataset, that is 0.908±0.016, 0.947±0.008, and 0.954±0.008 (in terms of mean value and standard deviation) in the JI, DC, and OC indicators, respectively. Moreover, the presented results show that our method obtains higher accuracy values when compared with GVF snake.

6 Conclusions and Future Work

This paper has proposed a new segmentation approach for CBCT images: The ADF snake for IAC segmentation and reconstruction. The algorithm has been exhaustively measured for three indicators including the Jaccard index, the Dice's coefficient,and the Overlap coefficient. All results indicate achieving of accuracy and thus providing reliable information to computer-aided programs in order to facilitate oral surgery. Future work will focus on full-automatic segmentation with no interfere of end users. Further testing of other segmentation methods is also needed in order to improve accuracy.

References

[1] N. L. Gerlach et al. Evaluation of the potential of automatic segmentation of the mandibular canal using cone-beam computed tomography. *British Journal of Oral and Maxillofacial Surgery*, 52(9):838 – 844, 2014.

[2] N. Hanssen et al. Nerves - level sets for interactive 3d segmentation of nerve channels. In *Biomedical Imaging: Nano to Macro, 2004. IEEE International Symposium on*, pages 201–204 Vol. 1, April 2004.

[3] W. Jerjes et al. Risk factors associated with injury to the inferior alveolar and lingual nerves following third molar surgeryrevisited. *Oral Surgery, Oral Medicine, Oral Pathology, Oral Radiology, and Endodontology*, 109(3):335 – 345, 2010.

[4] M. Kass, A. Witkin, and D. Terzopoulos. Snakes: Active contour models. *International journal of computer vision*, 1(4):321–331, 1988.

[5] G. Kim et al. Automatic extraction of inferior alveolar nerve canal using feature-enhancing panoramic volume rendering. *Biomedical Engineering, IEEE Transactions on*, 58(2):253–264, Feb 2011.

[6] T. Kondo, S. Ong, and K. W. Foong. Computer-based extraction of the inferior alveolar nerve canal in 3-d space. *Computer Methods and Programs in Biomedicine*, 76(3):181 – 191, 2004.

[7] R. Llorns, V. Naranjo, F. Lpez, and M. Alcaiz. Jaw tissues segmentation in dental 3d {CT} images using fuzzy-connectedness and morphological processing. *Computer Methods and Programs in Biomedicine*, 108(2):832 – 843, 2012.

[8] National Electronics and Computer Technology Center: NECTEC. *DentiView version 3.0*, 2015 (accessed March 12, 2015). `http://dentiplan.nectec.or.th/index.php?option=com_content&view=article&id=53&Itemid=61&lang=en`.

[9] S. Saowapak. and N. Walita. Automatic detection of inferior alveolar nerve canals on ct images. In *Biomedical Circuits and Systems Conference, 2006. BioCAS 2006. IEEE*, pages 142–145, Nov 2006.

[10] W. C. Scarfe, A. G. Farman, and P. Sukovic. Clinical applications of cone-beam computed tomography in dental practice. *J Can Dent Assoc*, 72(1):75–80, 2006.

[11] S. Thongvigitmanee et al. Dentiiscan: The first cone-beam ct scanner for dental and maxillofacial imaging developed in thailand. In *Nuclear Science Symposium and Medical Imaging Conference (NSS/MIC), 2013 IEEE*, pages 1–3, Oct 2013.

[12] S. Thongvigitmanee et al. Radiation dose and accuracy analysis of newly developed cone-beam ct for dental and maxillofacial imaging. In *Engineering in Medicine and Biology Society (EMBC), 2013 35th Annual International Conference of the IEEE*, pages 2356–2359, July 2013.

[13] G. Tognola et al. Gradient-vector-flow snake method for quantitative image reconstruction applied to mandibular distraction surgery. *Instrumentation and Measurement, IEEE Transactions on*, 58(7):2087–2093, July 2009.

[14] Y. Wu, Y. Wang, and Y. Jia. Adaptive diffusion flow active contours for image segmentation. *Computer Vision and Image Understanding*, 117(10):1421 – 1435, 2013.

[15] C. Xu and J. L. Prince. Generalized gradient vector flow external forces for active contours. *Signal Processing*, 71(2):131 – 139, 1998.

[16] C. Xu and J. L. Prince. Snakes, shapes, and gradient vector flow. *IEEE Transactions on image processing*, 7(3):359–369, 1998.